

Structure, site-specific magnetism and magneto-transport properties of epitaxial D0_{22} $\text{Mn}_2\text{Fe}_x\text{Ga}$ thin films

Davide Betto,¹ Yong-Chang Lau,^{2,*} Kiril Borisov,² Kurt Kummer,¹
N.B. Brookes,¹ Plamen Stamenov,² J.M.D. Coey,² and Karsten Rode²

¹*European Synchrotron Radiation Facility, B.P. 220, 38043 Grenoble, France*

²*CRANN and AMBER, Trinity College, Dublin 2, Ireland*

(Dated: November 12, 2021)

Ferrimagnetic $\text{Mn}_2\text{Fe}_x\text{Ga}$ ($0.26 \leq x \leq 1.12$) thin films have been characterised by X-ray diffraction, SQUID magnetometry, X-ray absorption spectroscopy, X-ray magnetic circular dichroism and Mössbauer spectroscopy with the aim of determining the structure and site-specific magnetism of this tetragonal, D0_{22} -structure Heusler compound. High-quality epitaxial films with low RMS surface roughness (~ 0.6 nm) are grown by magnetron co-sputtering. The tetragonal distortion induces strong perpendicular magnetic anisotropy along the c -axis with a typical coercive field $\mu_0 H \sim 0.8$ T and an anisotropy field ranging from 6 to 8 T. Upon increasing the Fe content x , substantial uniaxial anisotropy, $K_u \geq 1.0 \text{ MJ m}^{-3}$ can be maintained over the full x range, while the magnetisation of the compound is reduced from 400 to 280 kA m^{-1} . The total magnetisation is almost entirely given by the sum of the spin moments originating from the ferrimagnetic Mn and Fe sublattices, with the latter being coupled ferromagnetically to one of the former. The orbital magnetic moments are practically quenched, and have negligible contributions to the magnetisation. The films with $x = 0.73$ exhibit a high anomalous Hall angle of 2.5% and a high Fermi-level spin polarisation, above 51%, as measured by point contact Andreev reflection. The Fe-substituted Mn_2Ga films are highly tunable with a unique combination of high anisotropy, low magnetisation, appreciable spin polarisation and low surface roughness, making them very strong candidates for thermally-stable spin-transfer-torque switching nanomagnets with lateral dimensions down to 10 nm.

I. INTRODUCTION

Magnetic materials that exhibit a combination of strong uniaxial anisotropy, low magnetisation and high spin polarisation are crucial for the development of magnetic tunnel junction (MTJ)-based spin-transfer torque (STT) memories and oscillators. The thermal stability of a memory cell is determined by the factor $\Delta = K_{\text{eff}}V/k_{\text{B}}T$ where K_{eff} , V and k_{B} are the effective anisotropy constant, the cell volume and the Boltzmann constant, respectively. $\Delta > 60$ is conventionally required for ten-year data retention. A thermally-stable storage element with lateral dimensions below 10 nm and a thickness of less than 3 nm therefore requires a material or structure with $K_{\text{eff}} \sim 1 \text{ MJ m}^{-3}$.

Currently, the most studied storage system is Ta/ultrathin CoFeB/MgO-based heterostructures where the perpendicular magnetic anisotropy (PMA) is obtained via the surface/interface anisotropy of CoFeB/MgO[1–3]. The structure exhibits a moderate $K_{\text{eff}} \sim 0.2 \text{ MJ m}^{-3}$, due to the competition between interface and shape anisotropy associated with the sizable magnetisation. K_{eff} can often be improved by introducing a second CoFeB/MgO interface in more complicated MgO/CoFeB/Ta/CoFeB/MgO structures[4]. Nevertheless, it has been shown that even the optimised MTJ structure is unstable for dimensions below 30 nm[5].

Novel materials with strong magnetocrystalline or strain-induced PMA are needed.

A number of Mn-based Heusler alloys crystallise in the tetragonal D0_{22} structure[6, 7]. It is a variant of the cubic $L2_1$ structure with reduced symmetry, where the lattice c parameter is increased, giving rise to strong magneto-crystalline anisotropy. The potential of this material class in STT applications was first highlighted by Balke *et al.*[8], based on the bulk properties of D0_{22} Mn_{3-x}Ga . This pioneering work has led to the growth and characterisation of Mn-Ga thin films with properties that fulfil all major requirements for STT applications, *i.e.*, strong uniaxial anisotropy[9], low magnetisation, high spin polarisation [10], low damping, and high resonance frequency[11, 12]. In addition, the magnetic properties have been shown to be tunable by atomic substitution[13]. Other examples of Mn-based tetragonal Heusler compounds with high PMA are Mn_3Ge [14], $\text{Mn}_{3-x}\text{Co}_x\text{Ga}$ [15, 16] and $\text{Mn}_2\text{Fe}_x\text{Ga}$ [17, 18]. A particular case to note is $\text{Mn}_2\text{Ru}_x\text{Ga}$, which has a moderate anisotropy energy ($K_{\text{eff}} \sim 40 \text{ kJ m}^{-3}$), but an extremely low magnetisation leading to a very high predicted resonance frequency[19–24].

Gasi *et al.*[17] have synthesised polycrystalline ingots of Mn_2FeGa , in both tetragonal and pseudo-cubic structures. However, the tetragonal samples exhibit an exchange-spring behaviour with low remanence and low magnetic anisotropy. This was attributed to the presence of two magnetic phases, possibly due to Mn-Fe atomic disorder. Recently, Niesen *et al.*[18] deposited Mn-Fe-Ga thin films with various compositions in both cubic and tetragonal phases. They found maximal coercivity

* Electronic mail: yongchang.lau@qspin.phys.s.u-tokyo.ac.jp ;
Present address: Department of Physics, The University of Tokyo, Bunkyo, Tokyo 113-0033, Japan

(1.8 T) for a $\text{Mn}_3\text{Fe}_{0.4}\text{Ga}$ composition.

Here we determine the structural, magnetic and magneto-transport properties of the tetragonally distorted Heusler alloy $\text{Mn}_2\text{Fe}_x\text{Ga}$ (MFG), with $0.26 \leq x \leq 1.12$, in the form of epitaxial thin films. We used X-ray diffraction (XRD), SQUID magnetometry and magnetotransport to characterise the overall features of the samples, while the use of synchrotron radiation-based XAS and XMCD, as well as Mössbauer spectroscopy, allowed us to distinguish between the different magnetic elements.

II. EXPERIMENTAL DETAILS

High-quality epitaxial $\text{Mn}_2\text{Fe}_x\text{Ga}$ films are grown on $10 \times 10 \text{ mm}^2$ single-crystal $\text{MgO}(001)$ substrates in an automated Shamrock-based sputtering cluster tool with a base pressure of 4×10^{-8} mbar. The substrate temperature is kept at $T_{\text{sub}} = 300^\circ\text{C}$. The Fe concentration x is varied from $x \sim 0.26$ to $x \sim 1.12$ by tuning the power of the Fe gun while keeping that of the Mn_2Ga gun fixed during co-sputtering. The growth time has been 30 min for all samples, and we obtain MFG films of thicknesses ranging from 41.5 nm to 50.5 nm, corresponding to an MFG growth rate of about 0.025 nm s^{-1} . The samples are then capped with 2 nm AlO_x to avoid oxidation. We find, from the X-ray reflectometry, that the film thickness increases linearly as a function of the Fe sputtering power, while the X-ray density remains practically constant. We hence estimate the Fe concentration in our samples, assuming *no* crystalline vacancies nor interstitials. We will further discuss the validity of such an assumption in Section III. Strictly speaking, the exact formula unit of $\text{Mn}_2\text{Fe}_x\text{Ga}$ should therefore always contain 4 atoms, e.g., $\text{Mn}_2\text{Fe}_{0.26}\text{Ga}$ should be written as $\text{Mn}_{2.46}\text{Fe}_{0.31}\text{Ga}_{1.23}$. We shall, for readability, keep the formula unit with only one variable x throughout the text, and implicitly normalise the atom count to 4 whenever necessary.

The crystal structure and lattice parameters have been determined by symmetrical $\theta - 2\theta$ scans and reciprocal space maps using a BRUKER D8 diffractometer. The primary beam optical path contains a Cu K_α X-ray tube with a Göbel mirror and a double-bounce channel-cut Ge(220) crystal monochromator followed by a 0.1 mm divergence slit. The detector is a 1D LynxEye. 2.5° Soller slits have been used on both the primary and secondary beam paths.

The macroscopic magnetic properties have been measured within a Quantum Design MPMS XL 5 SQUID magnetometer in the RSO sample transport ($\mu_0 H_{\text{max}} = \pm 5 \text{ T}$) and also in a Quantum Design PPMS system ($\mu_0 H_{\text{max}} = \pm 14 \text{ T}$) with a Vibrating Sample Magnetometer (VSM) insert. The temperature-dependent magneto-transport have been probed in the same setup. The Curie temperature has been measured using a SQUID oven insert. Point contact Andreev reflection (PCAR)

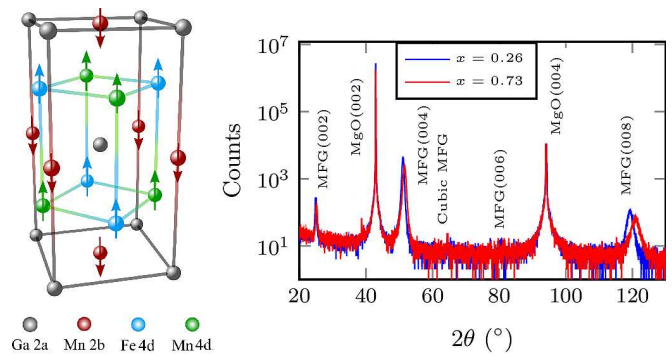


FIG. 1. Left: $D0_{22}$ crystal structure of Mn_2FeGa assuming perfect ordering. The arrows represent the orientation of the magnetic moments. Right: $\theta - 2\theta$ XRD scans of two MFG samples with different x values, confirming the $D0_{22}$ structure, with a fully developed (001) texture.

measurements[10, 25] have been performed within the PPMS system and also in a home-built setup using a Nb superconducting tip. Further details on the experimental setup and data analysis routine can be found elsewhere[26].

X-ray absorption spectroscopy (XAS) on the Mn and Fe $L_{2,3}$ edges has been carried out at the European Synchrotron Radiation Facility (ESRF) on the ID32 beamline[27] with both circular left and right polarisations in order to measure the X-ray magnetic circular dichroism (XMCD). These measurements have all been carried out at room temperature and in the longitudinal configuration, *i.e.* with the applied magnetic field $\mu_0 H = 9 \text{ T}$ collinear to the wave propagation vector \vec{k} . All measurements have been performed in both positive and negative applied magnetic fields.

Mössbauer spectroscopy was performed in conversion, at room temperature, using a WissEl (MA-260) electromagnetic Doppler drive system, a $^{57}\text{Co}(\text{Rh})$ gamma source, of actual activity $\sim 40 \text{ mCi}$ and $\text{He}(5\% \text{ methane})$ -gas phase proportional counter, operated at a fixed pressure of 1.50 bar, and a flow rate of approximately 30 sccm. Canberra amplification and discrimination electronics were used in conjunction with an in-house developed multi-parameter analyzer capable of recording simultaneously the Doppler velocity and escape energy for each detector event, up to a maximal resolution of 12×12 bits. α -Fe calibration spectra of 512 channels width, were also acquired to a level of approximately 10^7 counts per channel. Samples were mounted using silver-paint onto aluminium carriers. Custom folding, absorber geometry modelling, optimal escape energy selection and non-linear least squares regression routines were used for the extraction of the spectroscopic parameters and their statistical uncertainties. Isomer shifts are referred to the source.

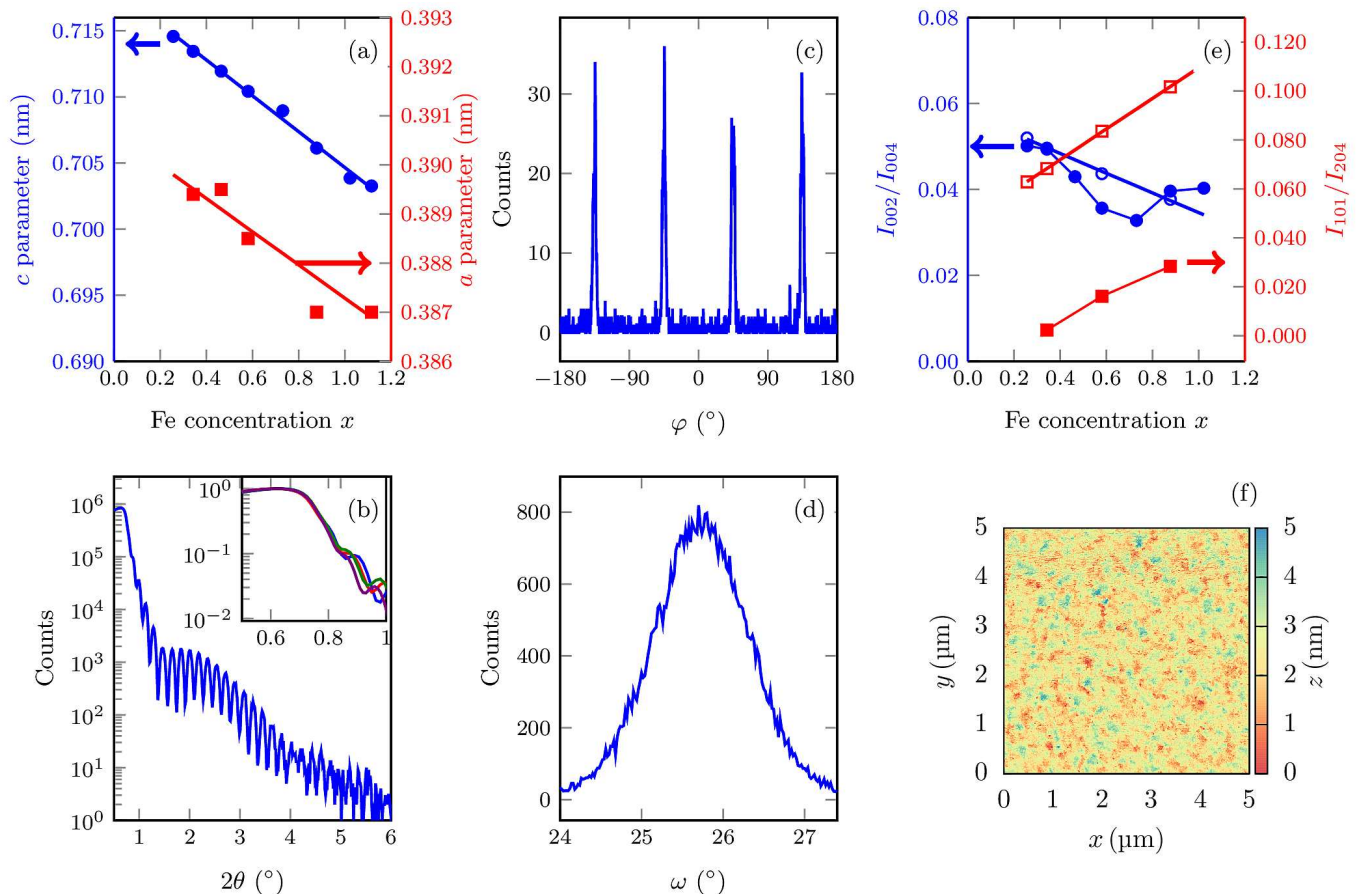


FIG. 2. (a) c and a lattice parameters as a function of Fe concentration x . Solid lines are linear regressions. (b) XRR scan of a $\text{Mn}_2\text{Fe}_{0.58}\text{Ga}$ thin film. The inset shows the normalised XRR scans of four MFG samples with x ranging from 0.26 to 1.02. The critical angle which is closely related to the X-ray density is independent of x . (c) φ XRD scan of MFG on the MFG(116) peak. (d) Rocking curve around the MFG(004) peak. (e) Experimental (filled symbols) and calculated (empty symbols) intensity ratios for the Bragg peaks as a function of the Fe concentration x . Solid lines are linear regressions of the calculated intensities. (f) AFM scan of an MFG sample.

III. EXPERIMENTAL RESULTS

A. Structural properties, X-ray diffraction and X-ray reflectivity

$\text{Mn}_2\text{Fe}_x\text{Ga}$ is expected to crystallise in the tetragonal $D0_{22}$ structure which belongs to the space group $139 (I4/mmm)$. The unit cell of a perfectly ordered stoichiometric Mn_2FeGa is illustrated in the left panel of Fig. 1. While the $2a$ Wyckoff position with an octahedral coordination is occupied by Ga, Fe atoms preferably fill the octahedral $4d$ sites. The $2b$ and the remaining $4d$ sites are filled by Mn atoms. If the Mn and Fe atoms at the $4d$ sites are ordered, as shown in Fig. 1, this Wyckoff position can be further separated into $2c$ and $2d$ sublattices. This leads to a structure with lower symmetry, corresponding to the space group $119 (I-4m2)$.

The two, crystallographically inequivalent, Mn sublattices ($2b$ and $4d$) have been predicted[28] to be antiferro-

magnetically coupled, in agreement with what has been experimentally confirmed in closely related compounds such as Mn_3Ga [29], $\text{Mn}_2\text{Ru}_x\text{Ga}$ [21] and Mn_2NiGa [30]. The Fe $4d$ sublattice has been predicted to be antiferromagnetically coupled to the Mn $2b$ sublattice and ferromagnetically coupled with the Mn $4d$ sublattice[28]. The overall magnetic structure of MFG can be approximated to that of a collinear ferrimagnet.

The $\theta - 2\theta$ symmetric X-ray diffraction data of MFG are shown in Fig. 1. All samples are highly textured with the c axis of the tetragonal unit cell along the film normal. The three diffraction peaks are indexed, in the $I4/mmm$ space group, MFG(002), MFG(004), and MFG(008). We find $a \sim 0.391$ nm and $c \sim 0.71$ nm, with both a and c decreasing monotonically with increasing x , as shown in Fig. 2. The ϕ scan at the MFG(116) reflection (Fig. 2(c)) confirms in-plane order. $\phi = 45^\circ$ corresponds to the $[110]$ direction of the MgO substrate, and we conclude that MFG crystallises in a “cube-on-

cube" fashion on the MgO(100) surface with the in-plane MgO [110] \parallel MFG [110]. In Fig. 2(d) we show the rocking curve of the MFG(004) peak with a full width at half maximum of $\sim 1.2^\circ$, indicating some degree of mosaicity, most probably due to the large lattice mismatch ($\sim 7.5\%$).

The D0₂₂ structure differs from the L1₀ by the ordering of the Ga atom at (0.5, 0.5, 0.5) fractional coordinates. The inter-plane ordering of Ga atoms can be estimated by the ordering parameter[29]:

$$S_{\text{inter-plane}} = \sqrt{(I_{002}^{\text{exp}}/I_{004}^{\text{exp}})/(I_{002}^{\text{cal}}/I_{004}^{\text{cal}})}, \quad (1)$$

while the intra-plane ($2a-2b$) ordering parameter is given by:

$$S_{\text{intra-plane}} = \sqrt{(I_{101}^{\text{exp}}/I_{204}^{\text{exp}})/(I_{101}^{\text{cal}}/I_{204}^{\text{cal}})} \quad (2)$$

where $I_{hkl}^{\text{exp(cal)}}$ is the experimental (calculated) intensity of the corresponding Bragg peak. In Fig. 2(e) we show the experimental intensity ratios as a function of Fe concentration, together with the expected values in the case of excess Ga atoms in the $2b$ position. The good agreement between the simulation and the experimental data for $S_{\text{inter-plane}}$ confirms that Ga is confined to the $2a-2b$ positions. The ordering of Ga at the centre of the unit cell is less marked, but still present and it increases with x . Due to the very similar atomic form factors of Mn and Fe, laboratory X-ray diffractometry is unable to discern the ordering among these two species.

Previously[29], we demonstrated that in manganese-deficient tetragonal Mn_{3-x}Ga films, the Ga vacancies are negligible and the Mn vacancies are distributed over the $2b$ and $4d$ sites, with a preference for the $2b$ positions. Here, we use the film density, determined from the X-ray reflectometry (XRR), as the key parameter to examine whether this can be applied to MFG. Using the experimental lattice parameters as inputs, we calculate the expected densities of MFG for $0.26 < x < 1.02$, assuming two extreme cases. First, we assume that deficiencies in Fe systematically lead to the formation of vacancies, *i.e.* similar to the case of Mn_{3-x}Ga. We find that the MFG density would increase from 5.9 g cm^{-3} for Mn₂Fe_{0.26}Ga to 7.4 g cm^{-3} for Mn₂Fe_{1.02}Ga. Second, we assume instead that the removal of Fe atoms induces a rearrangement of the atomic occupancy such that all atomic sites of the MFG are always fully occupied. In this second case, we find that the density depends only weakly on x and varies from 7.3 to 7.4 g cm^{-3} for $x = 0.26$ and $x = 1.02$, respectively.

In Fig. 2(b) we show a typical grazing-incident XRR scan of a Mn₂Fe_{0.58}Ga film. Best fit to the experimental data yields an X-ray density of $7.6(1) \text{ g cm}^{-3}$ and a low roughness of $\sim 0.5 \text{ nm}$. In the inset of Fig. 2(b), we show a zoom of the critical angle region of the XRR scans of four MFG films with x ranging from 0.26 to 1.02. The critical angle is the same for all four samples, indicating that their density is almost constant, regardless of

TABLE I. Site occupancy as a function of Fe concentration x

x	Ga $2a$	Ga $2b$	Mn $2b$	Mn $4d$	Fe $4d$
0.26	2.00	0.45	1.55	3.36	0.63
0.46	2.00	0.31	1.69	2.94	1.06
0.73	2.00	0.14	1.86	2.43	1.57
1.00	2.00	0.00	2.00	2.00	2.00

the value of x . This observation is in better agreement with the calculated x dependence of the density, assuming that all atomic sites of the MFG are fully occupied. The slightly higher experimental density may be due to the different sputter yield of Mn and Ga leading to a ratio lower than 2, similar to what found in another Mn-Ga based Heusler, doped with Ru[22, 23]. Excess Ga in the $2b$ positions then explains the lower intra-plane order parameter of MFG. Following the structural model outlined above, the site occupancy of some of the samples is reported in Tab. I.

Thin-film surface/interface quality and roughness are important parameters for integration in spin-electronic device stacks. We recorded tapping mode AFM images of the MFG surface. The surface of the film is smooth and free of pinholes (Fig. 2(f)), despite the high crystallinity of MFG and the large lattice mismatch with the substrate. The extracted RMS roughness of about 0.6 nm is in good agreement with the XRR fits. The surface roughness of the films might be further optimised by using lattice-matched substrate (e.g. SrTiO₃) or appropriate seed layers (e.g. Pt(001) and IrMn(001))[10, 31]. We note that the low roughness of MFG is in contrast with D0₂₂-Mn₃Ga films grown directly on MgO under similar conditions, which exhibit discontinuous island-like morphology[10]. We attribute this to the Fe incorporation that significantly improves the surface wetting of Mn-Ga alloys on MgO substrate. We further speculate that the change of the film morphology/wettability between Mn₂Mn_xGa and Mn₂Fe_xGa is closely linked to the different tendencies for creating vacancies or antisites when the two compounds are off-stoichiometric ($x < 1$).

B. Magnetic and magneto-transport properties

In Fig. 3(a) we plot the M - H loops of a Mn₂Fe_{0.73}Ga film, measured at 300 K with in-plane $\mu_0 H_{\parallel}$ and out-of-plane $\mu_0 H_{\perp}$ applied fields. The sample exhibits strong PMA with a low saturation magnetisation $M_s = 320 \text{ kA m}^{-1}$, a coercive field of 0.85 T and a high remanence ratio of $\sim 90\%$. From the hard-axis M - H loop, we extract an anisotropy field $\mu_0 H_{\text{an}} = 6.5 \text{ T}$. Using $K_{\text{eff}} \approx M_s H_{\text{an}}/2$ we estimate an effective anisotropy constant K_{eff} that exceeds 1 MJ m^{-3} . We find that the general shape of the hysteresis loop and the high $K_{\text{eff}} \geq 1 \text{ MJ m}^{-3}$ are maintained for MFG films with x ranging from 0.26 to 1.02. We should also note that a soft in-plane component is systematically found in the

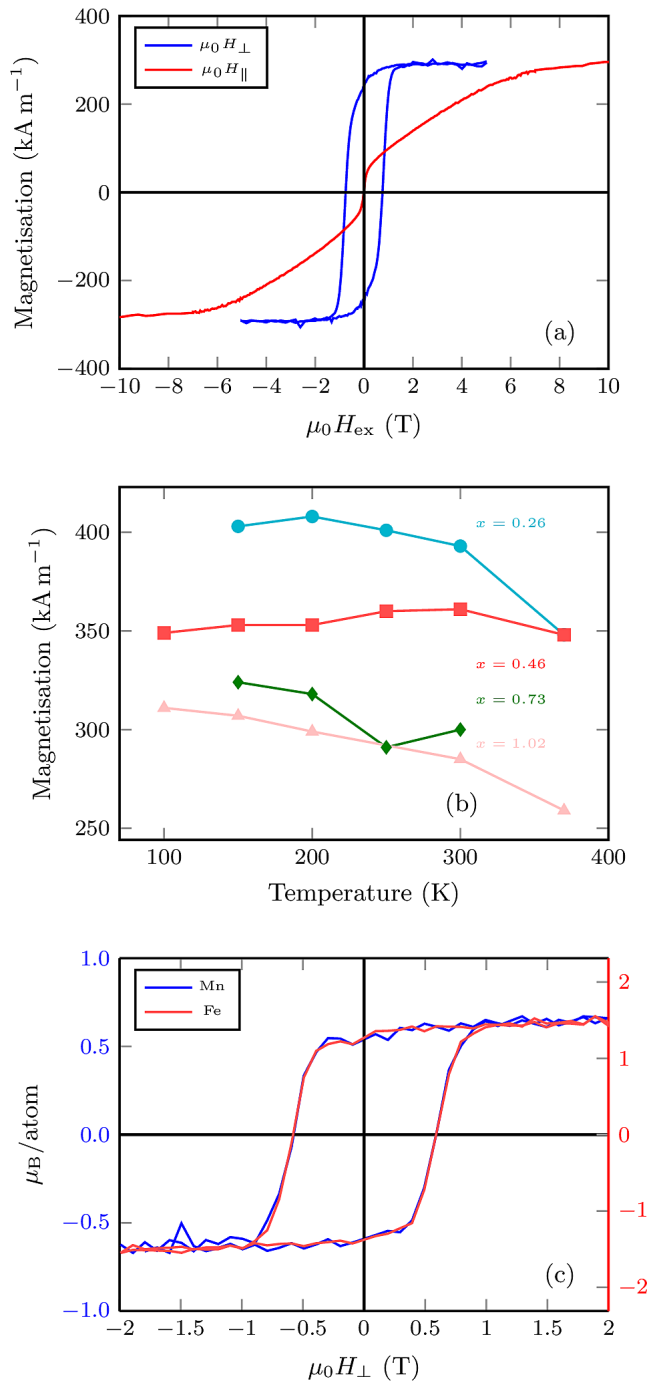


FIG. 3. (a) Typical out-of-plane and in-plane M - H loops of a $\text{Mn}_2\text{Fe}_{0.73}\text{Ga}$ film. (b) Temperature dependence of the magnetisation of MFG films with 4 different Fe concentrations. (c) Element-specific hysteresis loops obtained from the XMCD signal of a MFG sample with $x = 0.26$.

hard M - H_{\parallel} loops of MFG with various Fe concentrations. Previously, similar observations in tetragonal Mn_{3-x}Ga were attributed to the oscillatory exchange coupling between the first and second nearest Mn neighbours[29].

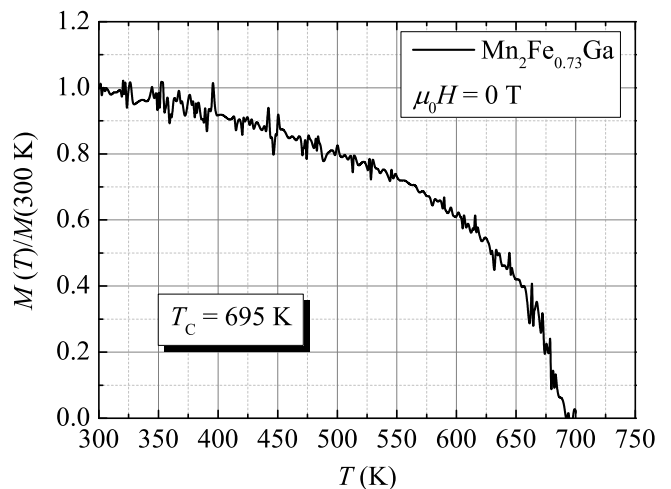


FIG. 4. SQUID magnetometry of a $\text{Mn}_2\text{Fe}_{0.73}\text{Ga}$ film in the oven insert. The sample was saturated out-of-plane at 300 K, set in remanence and measured while heating up. The curve is normalized to its value at 300 K. The extracted Curie temperature is 695 K.

Our experimental observations suggest that similar situation is likely to happen in MFG, even in the presence of the additional magnetic Fe atoms. This soft component is not observed in anomalous Hall effect loops recorded on the same samples, as Mn in the $2b$ positions contribute only marginally to the Fermi-level density of states[23]. In Fig. 3(b), we show the temperature dependence of the saturation magnetisation for samples with different x . The MFG magnetisation at room temperature decreases from 400 to 280 kA m^{-1} with increasing Fe doping. The similar temperature dependence of the magnetisation suggests that the Curie temperature of these compounds with varying x remains to be well above the room temperature.

The Curie temperature of a $\text{Mn}_2\text{Fe}_{0.73}\text{Ga}$ thin film has been directly measured using SQUID magnetometry with an oven insert. The sample magnetisation was first saturated at 300 K using an out-of-plane 5 T field and left in remanent state. The remanent magnetisation was measured while warming up the sample, as shown in Fig. 4. The extracted Curie temperature is 695 K. The sample was then cooled to $T = 300$ K and a full hysteresis loop was recorded. No changes in magnetic properties were observed. We therefore conclude that the heat treatment does not affect the magnetic properties of MFG and the extracted Curie temperature is not due to irreversible structural change from D0_{22} (tetragonal-ferrimagnetic) to D0_{19} (hexagonal-antiferromagnetic).

The magneto-transport of unpatterned MFG films are measured in standard Van der Pauw geometry. The transverse resistivity ρ_{xy} as a function of $\mu_0 H_{\perp}$ at 300 K for MFG films with x ranging from 0.26 to 1.12 are plotted in Fig. 5(a). The $\rho_{xy}(\mu_0 H_{\perp})$ hysteresis loops are dominated by the anomalous Hall effect contribu-

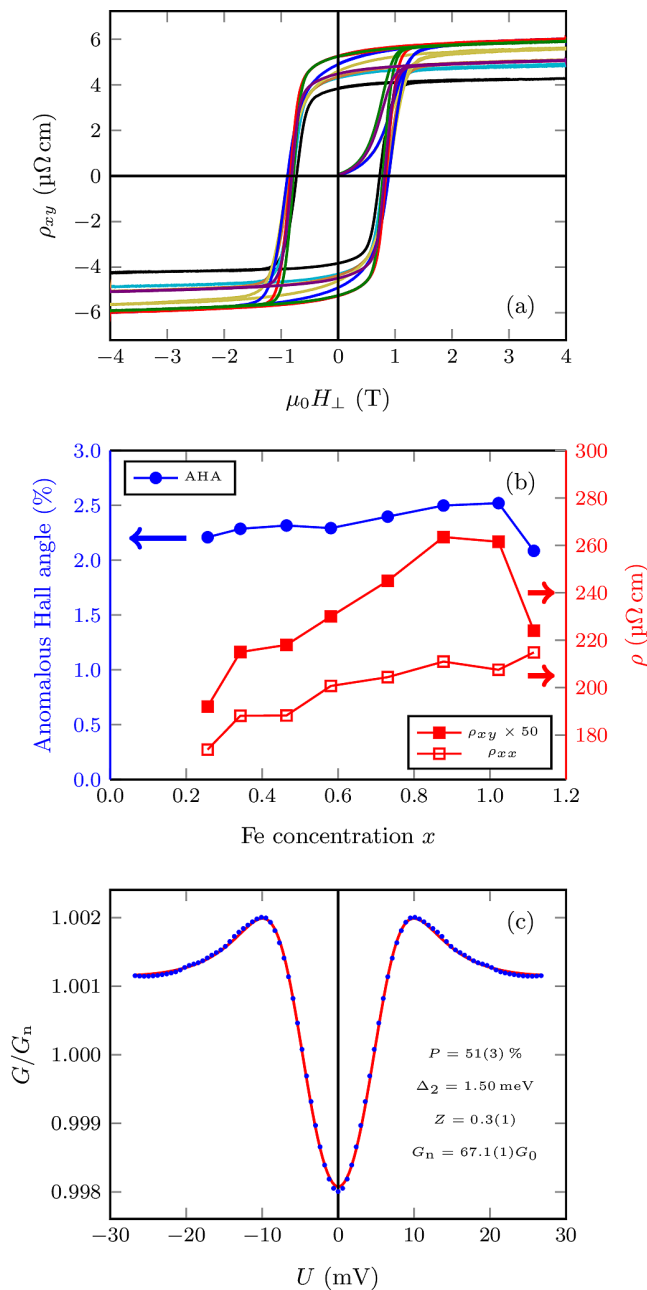


FIG. 5. (a) Anomalous Hall effect hysteresis loops for samples with different Fe concentration x as a function of the out-of-plane external field $\mu_0 H_{\perp}$. (b) Anomalous Hall angle, ρ_{xy} and ρ_{xx} at room temperature as a function of the Fe concentration x . (c) Point contact Andreev reflection spectroscopy of MFG with $x = 0.73$. The red line is a fit using the parameters listed in the figure. For details see Ref.[32].

tion and corroborate the $M - H$ loops obtained from the SQUID magnetometry. The longitudinal resistivity ρ_{xx} , the transverse resistivity at remanence ρ_{xy} and the anomalous Hall angle (AHA), *i.e.* the ρ_{xy}/ρ_{xx} ratio, of these samples at room temperature are summarised in Fig. 5(b). ρ_{xx} increases with increasing x which may be

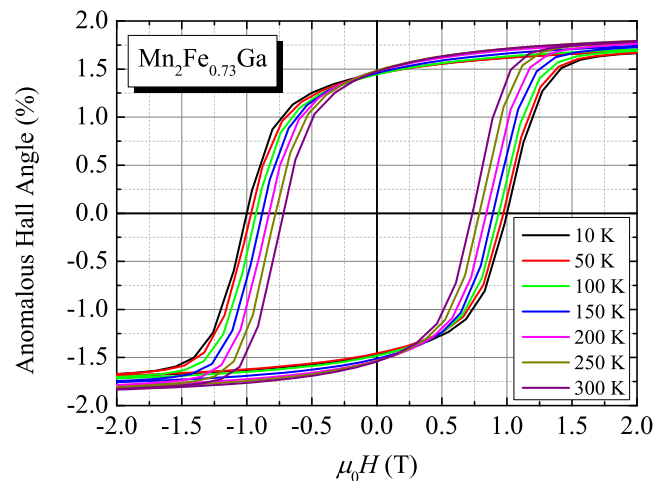


FIG. 6. Anomalous Hall effect loops for a $\text{Mn}_2\text{Fe}_{0.73}\text{Ga}$ film at various temperatures ranging from 10 to 300 K. Each curve was measured up to ± 5 T but only data within ± 2 T range are shown.

attributed to the enhanced scattering causing by the additional Fe atoms. ρ_{xy} exhibits similar but steeper dependence with varying x , leading to a moderate increase of AHA up to $x = 1.02$. We highlight that AHA is about 2.5% at $x = 1.02$, which is comparable to other Mn-Ga based compounds [20, 33] and is an order of magnitude higher than the AHA normally found in 3d transition metal ferromagnets[34]. This value would be even larger if MFG can be further optimised to achieve full remanence.

A linear regression of $\log(\rho_{xy})$ versus $\log(\rho_{xx})$ yields $\rho_{xy} \propto \rho_{xx}^{1.6}$, which is typically found in weakly localised bad metals[35]. The high AHA is indicative of a strong intrinsic contribution (related to Berry phase curvature) and/or a high spin polarisation at the Fermi level. Although the tetragonally distorted, Mn-based Heusler alloys have not been predicated to be half-metallic (100% spin polarisation) unlike their cubic cousins[28, 36], a pseudo-spin-gap has been theoretically predicted and experimentally observed[10]. To further elucidate the origin of the high AHA, we have measured Point Contact Andreev Reflection (PCAR) [32] for a MFG film with $x = 0.73$. A typical PCAR spectrum is shown in Fig. 5(c), for which data analysis following the work of Strijkers *et al*[26, 37] yields a high spin polarisation $P = 51\%$. This is the highest spin polarisation measured among all D0_{22} compounds, excluding Mn_3Ga which, in the tetragonal form, is metastable and often forms rough and non-continuous films. The ease of growing continuous and smooth MFG films may prove to be more important than achieving the highest possible spin polarisation for future spin-electronic device structures.

The temperature dependence of the anomalous Hall effect loops for $\text{Mn}_2\text{Fe}_{0.73}\text{Ga}$ is plotted in Fig. 6. The magnitude of ρ_{xy} is practically temperature independent, with only slight increase of the coercivity at lower tem-

peratures. These observations indicate little Fermi level spin polarisation degradation with increasing temperature and demonstrate the high robustness of the PMA due to the tetragonal $D0_{22}$ structure. It is worth noting that the magnetism and the transport properties of the tetragonal Mn_2Fe_xGa differ significantly from those of the near-cubic Mn_2Ru_xGa , despite the fact that the total valence electron of both systems increases from 17 to 25 when x is varied from 0 to 1. Notably, Mn_2Ru_xGa possesses a highly tunable magnetic compensation point where both the magnetisation and the anomalous Hall effect change sign[19, 20]. This can be understood by considering the famous 18 and 24 valence electron counting rule which is valid for half-metallic cubic half-Heusler and full Heusler compounds, respectively[38, 39]. Here, we find that such unique properties are absent in tetragonal MFG. Our findings are in better agreement with the theoretical prediction that the magnetism in tetragonal Heuslers approximately obeys a “25.7” valence electron counting rule[28]. The model predicts $-0.7 \mu_B \text{ f.u.}^{-1}$ for $D0_{22}$ Mn_2Fe_1Ga , while we obtain $-1.8 \mu_B \text{ f.u.}^{-1}$ at 100 K.

C. X-ray absorption and magnetic circular dichroism

XMCD is the method of choice for determining the element-specific spin and orbital angular momenta in complex thin film systems. We measured XAS and XMCD at the $L_{3,2}$ edges of Mn and Fe (corresponding to the electronic transition $2p^63d^n \rightarrow 2p^53d^{n+1}$) for four samples with $x = 0.26, 0.46, 0.73$ and 1.02 . The incident beam \vec{k} -vector has been kept parallel to the applied magnetic field and at an angle θ with the sample normal, hence $\theta = 0^\circ$ corresponds to normal incidence. All data are recorded by detection of the total electron yield (TEY). Saturation effects have not been taken into account since, for the worst case scenario of Mn_2Fe_1Ga , the ratio between the electron escape depth and the X-ray absorption length at the maximum incident angle used, $\lambda_e/\lambda_x \cos \theta$, is estimated to be ~ 0.03 , resulting in a correction of about 2%[40, 41].

We first concentrate on the element-specific hysteresis loops of MFG, measured on the L_3 edges of Mn and Fe. We find that the Fe and the net Mn moments are strongly and ferromagnetically coupled, with superimposed hysteresis loops (see Fig. 3(c)) for all values of x , in agreement with the collinear magnetic mode described above.

In Fig. 7 we show absorption and dichroism spectra at the Mn and Fe L edges. The broad and featureless XAS spectral shape indicates that both ions are in a metallic environment. Upon increasing x (addition of Fe), the Mn XMCD spectra become increasingly more structured, indicative of increased electronic localisation. The Fe XMCD spectra on the other hand remain broad and metallic-like. It has been shown[42] that Mn atoms

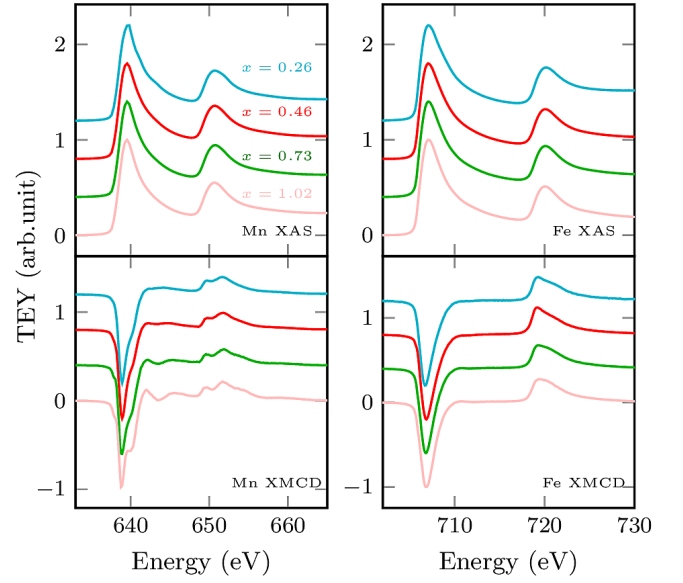


FIG. 7. XAS and XMCD spectra for Mn and Fe at normal incidence for samples with different Fe concentration x . The XAS spectra are normalised to unity in the post-edge region. The XMCD spectra are normalised to unity in order to better appreciate the changes in the shape. All spectra are shifted for clarity.

in the $2b$ positions are more localised than those in the $4d$ sublattices, which are expected to be of almost completely itinerant nature. This corroborates our structural model where Fe occupies mainly a subset of the $4d$ positions, while Mn occupies both $2b$ and $4d$. As x increases, $4d$ is progressively emptied of Mn (filled by Fe), and the ratio of Mn occupying $2b$ increases, resulting in increased Mn localisation.

We now turn to the orbital and spin moments of Fe and Mn as a function of x and θ . The expectation values of the spin $\langle S \rangle$, orbital $\langle L \rangle$ and magnetic dipole moment $\langle T \rangle$ were determined using the magneto-optical sum rules[43], from which we infer the spin, orbital and dipolar moments.

From the uniaxial anisotropy constant K_u and the saturation magnetisation, determined by magnetometry, we find that the sample magnetisation can be saturated in the direction θ in an applied field of 9 T, available at the beamline. We can therefore determine the effective spin $m_{S_{\text{eff}}} = m_S + 7m_T$ and orbital m_L moments, where m_S and m_T are the spin and magnetic dipole moments, respectively. At saturation, the spin moment is parallel to the applied field, whereas the orbital and dipole momenta may remain at an angle. The effective spin moment as a function of incidence angle θ is:[44]

$$m_S + 7m_T^\theta = m_S + 7(m_T^\perp \cos^2 \theta + m_T^\parallel \sin^2 \theta) \quad (3)$$

where m_T^\perp and m_T^\parallel are the out-of-plane and in-plane components of the magnetic dipole moment. In particular,

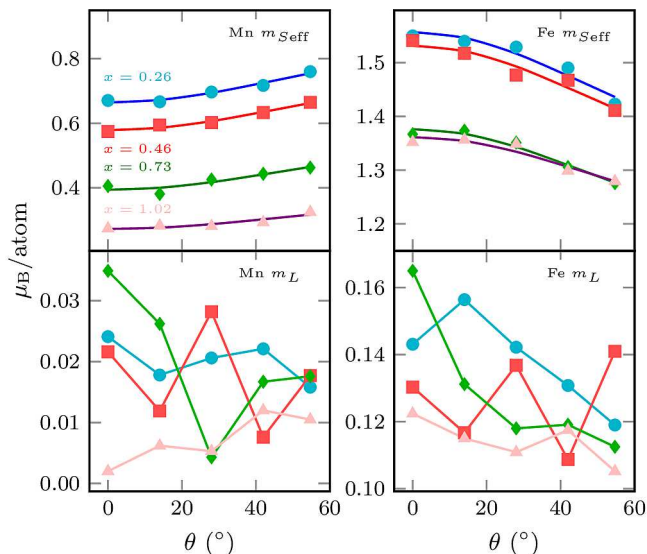


FIG. 8. Effective spin and orbital moments of the Mn and Fe sublattices as a function of the incidence angle of the beam k -vector and field direction. Solid lines in the $m_{S_{\text{eff}}}$ plots are fits using eq. 3.

we recorded spectra at the ‘magic’ angle $\theta = 54.6^\circ$, where $m_T^\perp + 2m_T^\parallel = 0$ for point group symmetries higher than D_{4h} and therefore $m_{S_{\text{eff}}} = m_S$ [45].

The effective spin and orbital momenta determined via the sum rules are shown as a function of incidence angle θ in Fig. 8. The solid lines in the upper panels are fits to the experimental values using Eq. 3. We find average values of m_T^\parallel of ~ 0.005 and $\sim -0.008 \mu_B/\text{atom}$ for Mn and Fe, respectively, while the average values of m_T^\perp are ~ -0.010 and $\sim 0.015 \mu_B/\text{atom}$. One can show[45] that for more than half-filled $3d$ shells, a positive (negative) value of m_T^\parallel (m_T^\perp) corresponds to octahedral (tetrahedral) coordination with tetragonal distortion, which is consistent with our structural model. Upon combining the net moments from the sum rules and the Fe content x , we have verified that the resulting net magnetisation for the four samples are in reasonable agreement with those obtained from the magnetometry, which validates our structural and compositional analyses in Section III A. Ga, as expected, gives rise to negligible contribution to the magnetisation.

The orbital moments are weak, as expected for ions in a tetragonal environment, and decrease as θ increases, except for Mn when $x > 1$. The anisotropy of the orbital momenta is a direct consequence of magnetocrystalline anisotropy[46], so that the higher orbital moment is observed along the easy axis of the local environment. From the angular dependence of m_L , we infer that the Fe positions ($4d$), exhibit easy- c -axis anisotropy. Mn is present in both the $4d$ and $2b$ positions, and for $x > 1$, the anisotropy constant changes sign, going from easy-axis to easy plane. We have previously found[29] that for Mn_3Ga

TABLE II. Average site-specific spin moments m_S and uniaxial anisotropies K_u . K_u in units of MJ m^{-3} are calculated for Mn_2FeGa .

	Mn $4d$	Mn $2b$	Fe $4d$	Fe $2b$
100% Fe $4d$ occupancy				
m_S (μ_B/atom)	1.5	0.9	1.4	-
K_u (meV/atom)	0.37	-0.46	0.42	-
K_u (MJ m^{-3})	1.1	-1.4	1.3	-
80% Fe $4d$ occupancy				
m_S (μ_B/atom)	1.9	2.1	2.1	2.0
K_u (meV/atom)	0.50	-0.86	0.53	-0.11
K_u (MJ m^{-3})	1.8	-2.1	1.3	-0.06

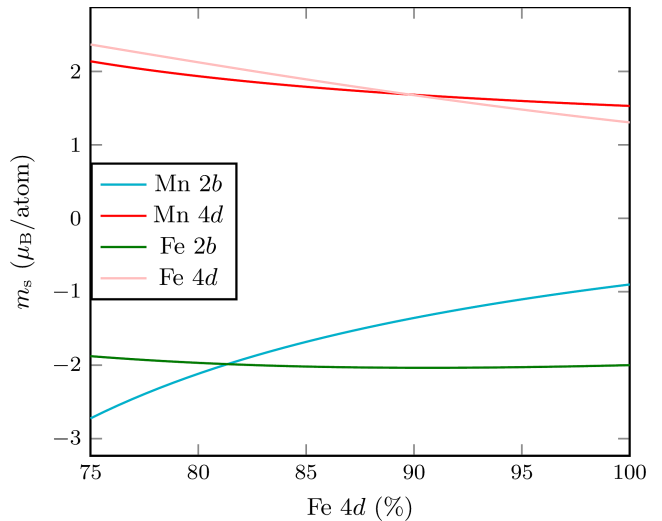


FIG. 9. Site-specific moment as a function of the occupancy percentage of Fe atoms in the $4d$ site.

the $4d$ site has perpendicular anisotropy, while the $2b$ site possesses in-plane anisotropy. Therefore, when the Mn $2b$ occupation is sufficiently high, the net magnetocrystalline anisotropy of Mn changes from easy-axis (due to $4d$), to easy-plane (due to $2b$) in MFG.

Using the results from the sum rules and the magnetometry, we attempt to estimate the average site-specific magnetic moments and uniaxial anisotropies in MFG, assuming that they remain constant with increasing Fe dopant occupying $4d$ sites. The magnetocrystalline anisotropy derives from the second-order correction in the energy due to the spin-orbit coupling when m_S is rotated from parallel to perpendicular to the out-of-plane easy axis. It has been evaluated using the Bruno model[47, 48] and estimating the change in orbital moment from the equation[44]:

$$m_L^\theta = m_L^\perp \cos^2 \theta + m_L^\parallel \sin^2 \theta. \quad (4)$$

The average site-specific K_u per atom are then renormalised by the site occupancy and the volume of Mn_2FeGa . Results are reported in Tab. II.

Although adequate in describing the macroscopic prop-

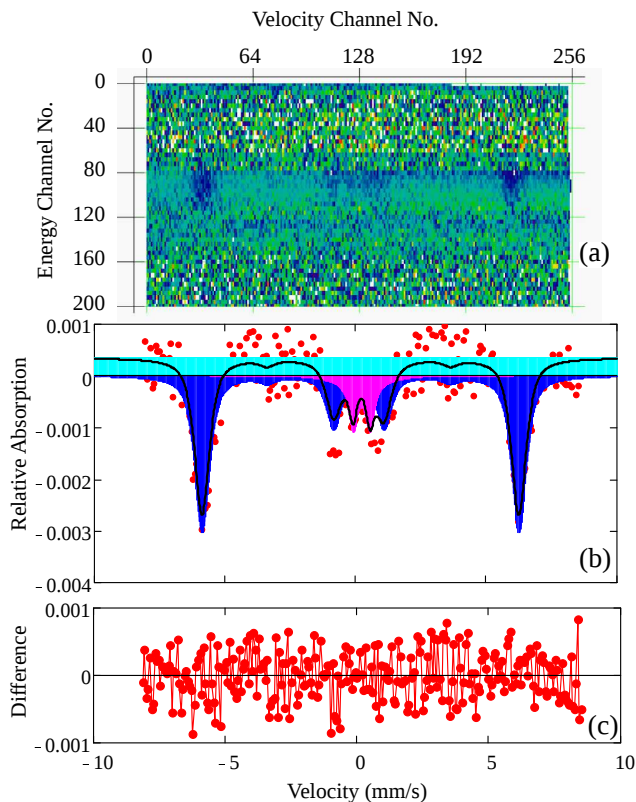


FIG. 10. (a): Pre-processed two-dimensional Mössbauer data. (b) Optimal velocity spectrum and two-component fit. (c) Spectrum-fit difference.

erties of the MFG system, this simple model, that assumes a perfectly ordered crystal, leads to a higher Mn $4d$ moment than that of the Mn $2b$, in contrast with earlier reports[29] and with the fact that the $3d$ shell of Mn in $2b$ sites is more localised than that of Mn in $4d$ sublattices. We believe that this is due to the presence of a small amount of Fe $2b$ antisites. In order to elucidate the consequences due to possible Fe disorder, we show in Fig. 9 the site-specific magnetic moments assuming a certain percentage of Fe atoms occupying the $2b$ site and coupled antiferromagnetically with their $4d$ counterparts. We find that the Mn $2b$ moment increases more rapidly with increasing Fe disorder and eventually surpasses the Mn $4d$ moment when about 20% of Fe are in $2b$ sites. In addition, the site-specific Mn moments increases towards the expected values of $\sim 2 \mu_B$ [29]. This degree of Fe site-disorder may explain our Mössbauer results in the following section.

D. Mössbauer spectroscopy

In order to verify the microscopic magnetic order of the system, Mössbauer spectra have been acquired in the conversion electron geometry on the $\text{Mn}_2\text{Fe}_{0.75}\text{Ga}$ sample. The multi-parameter analyzer allows for the optimal

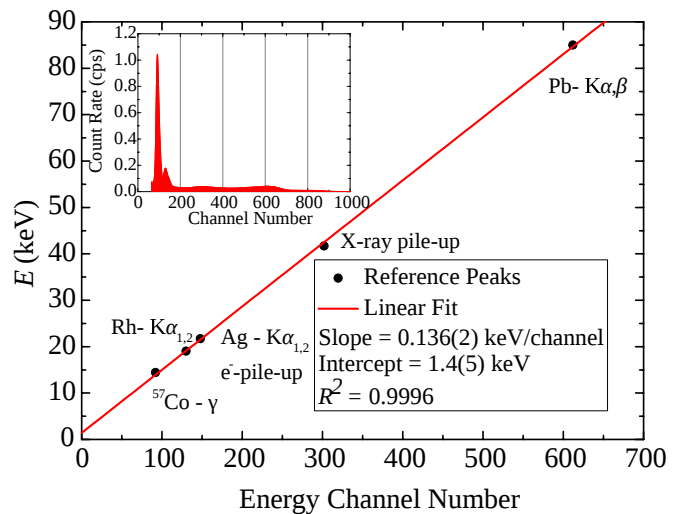


FIG. 11. Assignment of characteristic X-ray lines for Mössbauer and calibration. Inset: integral energy spectrum.

software discrimination and weighting of what is otherwise a rather weak absorption from the sub-percent natural Fe^{57} content. The pre-processed two-dimensional data are shown in Fig. 10 (a). There is a single well-defined absorption contrast corresponding to the energy of the incoming gamma rays (centred around energy channel 90). The clear sextet corresponds to magnetically ordered iron oriented predominantly out-of-plane. In order to confirm the assignment of the observed signal, the integral energy spectrum, as represented on the inset of Fig. 11, is interpreted in terms of the various gamma and characteristic X-ray lines present. The assignment and calibration are visualized in Fig. 11.

The optimal velocity spectrum is shown on Fig. 10 (b), together with a two-component fit to it. The two components are attributed to ordered out-of-plane metallic iron in a slightly distorted local environment (effective hyperfine field of $37.7(1)$ T) and paramagnetic (or in-plane magnetised with a low ordering temperature, in close to Fe^{3+} configuration). Approximately 85% of the iron content is ordered at room temperature, which agrees well with the measured, by SQUID magnetometry, Curie temperature of 695 K and the shape of the $M(T)$ curve. The detailed fitting parameters are listed in Tab. III, with their statistical errors included in brackets. In details, the parameters are: Γ = Lorentzian FWHM, σ = Gaussian standard deviation, μ = weighting factor in the pseudo-Voigt lineshape ($\mu\text{Lorentz} + (1 - \mu)\text{Gauss}$), δ = isomer shift, $\Delta/6$ = electric quadrupole moment, B_{hf} = hyperfine field, Θ = average angle between the surface normal (the gamma beam direction) and the local magnetisation. The 40 nm thick sample did sustain discharge damage in the course of the first two weeks of data acquisition. No magnetic Mössbauer signature was resolvable in three subsequent one-month-long data runs at both high and low detector pressure of the same sample.

TABLE III. Fitting parameters for the Mössbauer spectrum

Model	Area (%)	Γ (mm s ⁻¹)	σ (mm s ⁻¹)	μ	δ (mm s ⁻¹)	$\Delta/6$ (mm s ⁻¹)	B_{hf} (T)	Θ (rad)
Ferro. sextet	84.9	0.6(2)	0.3(2)	0.8	0.15(3)	0.01(1)	37.7(1)	0.2(1)
Para. doublet	15.1	0.4(1)	1(2)	0.8	0.22(5)	0.11(2)	0	-

IV. CONCLUSIONS

In summary, the structural, magnetic and magneto-transport properties of ferrimagnetic Mn₂Fe_xGa films have been experimentally investigated. This ternary compound crystallises in the tetragonally-distorted D0₂₂ structure, which results in high perpendicular anisotropy ($K_u \geq 1.0 \text{ MJ m}^{-3}$) with a high in-plane anisotropy field exceeding 6 T. The ferrimagnetic spin structure leads to low net magnetisation at room temperature, which is tunable from 400 to 280 kA m⁻¹ with increasing Fe content. The thin films are smooth and pinhole-free, with a RMS roughness of $\sim 0.6 \text{ nm}$. The anomalous Hall angle as high as $\sim 2.5\%$ has been interpreted as a sign of high spin polarisation. This has been confirmed by PCAR spectroscopy, which shows an appreciable 51% transport spin polarisation on the same sample. Using X-ray absorption spectroscopies, the magnitude and coupling of the spin and orbital magnetic moments for each element have been determined. The element-specific characterisation of the moments and the angular dependence allow us to propose a model for the evolution of the magnetic structure and the site occupancy with x . This model with $\sim 20\%$ of Fe antisites in $2b$ sublattices is corroborated by the Mössbauer spectra.

In ferrimagnetic materials, the precession of the magnetisation presents two characteristics resonance modes. The lower frequency mode, also called the ferromagnetic mode, occurs when the magnetic moments of the two antiferromagnetically-coupled sublattices precess together as a single, lower amplitude, moment. Its res-

onance frequency is[12] $f_- = \gamma/2\pi(\mu_0 H_{\text{an}} - \mu_0 M_s) \sim 150 \text{ GHz}$, where γ is the gyromagnetic ratio. The higher frequency mode, or ferrimagnetic mode, is related to the exchange field and the site-specific moments and anisotropies of the sublattices. The exchange field can be approximated from the Curie temperature employing a simple mean-field model of ferrimagnetism and averaged nearest-neighbours interactions. Using an exchange field of $\sim 250 \text{ T}$, we estimate the resonance frequency of the ferrimagnetic mode f_+ to be above 10 THz[49]. In this case, we considered a sample of Mn₂Fe₁Ga and averaged the properties of Mn and Fe in the $4d$ sublattice. Interestingly, there seems to be no vacancies in the crystal structure for any value of x , contrarily to what has been found in Mn_{3-x}Ga[29].

In summary, Fe-doped Mn-Ga films exhibit the unique combination of outstanding magnetic and transport properties, in addition to low surface roughness. This novel material with perpendicular anisotropy is an exceptional candidate for spin-transfer-torque devices, such as memories and oscillators, with high thermal stability down to 10 nm and ferromagnetic resonance frequency of about 150 GHz.

ACKNOWLEDGMENTS

D.B., Y.-C.L., K.R. and J.M.D.C. acknowledge the funding by the SFI through AMBER and grant 13/ERC/12561. K.B. and P.S. acknowledge financial support from Science Foundation Ireland (SFI) within SSPP (11/SIRG/I2130).

-
- [1] S. Ikeda, K. Miura, H. Yamamoto, K. Mizunuma, H. D. Gan, M. Endo, S. Kanai, J. Hayakawa, F. Matsukura, and H. Ohno, *Nature Materials* **9**, 721 (2010), 10.1038/nmat2804.
 - [2] D. C. Worledge, G. Hu, D. W. Abraham, J. Z. Sun, P. L. Trouilloud, J. Nowak, S. Brown, M. C. Gaidis, E. J. O'Sullivan, and R. P. Robertazzi, *Applied Physics Letters* **98**, 022501 (2011).
 - [3] H. D. Gan, H. Sato, M. Yamanouchi, S. Ikeda, K. Miura, R. Koizumi, F. Matsukura, and H. Ohno, *Applied Physics Letters* **99**, 252507 (2011).
 - [4] H. Sato, M. Yamanouchi, S. Ikeda, S. Fukami, F. Matsukura, and H. Ohno, *Applied Physics Letters* **101**, 022414 (2012), <http://dx.doi.org/10.1063/1.4736727>.
 - [5] H. Sato, E. C. I. Enobio, M. Yamanouchi, S. Ikeda, S. Fukami, S. Kanai, F. Matsukura, and H. Ohno, *Applied Physics Letters* **105**, 062403 (2014), <http://dx.doi.org/10.1063/1.4892924>.
 - [6] T. Graf, C. Felser, and S. S. Parkin, *Progress in Solid State Chemistry* **39**, 1 (2011).
 - [7] B. Balke, G. Fecher, and C. Felser, in *Spintronics*, edited by C. Felser and G. H. Fecher (Springer Netherlands, 2013) pp. 15–43.
 - [8] B. Balke, G. H. Fecher, J. Winterlik, and C. Felser, *Applied Physics Letters* **90**, 152504 (2007).
 - [9] F. Wu, S. Mizukami, D. Watanabe, H. Naganuma, M. Oogane, Y. Ando, and T. Miyazaki, *Applied Physics Letters* **94**, 122503 (2009), <http://dx.doi.org/10.1063/1.3108085>.
 - [10] H. Kurt, K. Rode, M. Venkatesan, P. Stamenov, and J. M. D. Coey, *Phys. Rev. B* **83**, 020405 (2011).
 - [11] S. Mizukami, F. Wu, A. Sakuma, J. Walowski, D. Watan-

- abe, T. Kubota, X. Zhang, H. Naganuma, M. Oogane, Y. Ando, and T. Miyazaki, *Phys. Rev. Lett.* **106**, 117201 (2011).
- [12] N. Awari, S. Kovalev, C. Fowley, K. Rode, R. A. Gallardo, Y.-C. Lau, D. Betto, N. Thiyagarajah, B. Green, O. Yildirim, J. Lindner, J. Fassbender, J. M. D. Coey, A. M. Deac, and M. Gensch, *Applied Physics Letters* **109**, 032403 (2016), <http://dx.doi.org/10.1063/1.4958855>.
- [13] J. Winterlik, S. Chadov, A. Gupta, V. Alijani, T. Gasi, K. Filsinger, B. Balke, G. H. Fecher, C. A. Jenkins, F. Casper, J. Kbler, G.-D. Liu, L. Gao, S. S. P. Parkin, and C. Felser, *Advanced Materials* **24**, 6283 (2012).
- [14] H. Kurt, N. Baadji, K. Rode, M. Venkatesan, P. Stamenov, S. Sanvito, and J. M. D. Coey, *Applied Physics Letters* **101**, 132410 (2012).
- [15] S. Ouardi, T. Kubota, G. H. Fecher, R. Stinshoff, S. Mizukami, T. Miyazaki, E. Ikenaga, and C. Felser, *Applied Physics Letters* **101**, 242406 (2012), <http://dx.doi.org/10.1063/1.4770303>.
- [16] C. Fowley, S. Ouardi, T. Kubota, O. Yildirim, A. Neudert, K. Lenz, V. Sluka, J. Lindner, J. M. Law, S. Mizukami, G. H. Fecher, C. Felser, and A. M. Deac, *Journal of Physics D: Applied Physics* **48**, 164006 (2015).
- [17] T. Gasi, A. K. Nayak, J. Winterlik, V. Ksenofontov, P. Adler, M. Nicklas, and C. Felser, *Applied Physics Letters* **102**, 202402 (2013), <http://dx.doi.org/10.1063/1.4807427>.
- [18] A. Niesen, C. Sterwerf, M. Glas, J. M. Schmalhorst, and G. Reiss, *IEEE Transactions on Magnetics* **PP**, 1 (2016).
- [19] H. Kurt, K. Rode, P. Stamenov, M. Venkatesan, Y.-C. Lau, E. Fonda, and J. M. D. Coey, *Phys. Rev. Lett.* **112**, 027201 (2014).
- [20] N. Thiyagarajah, Y.-C. Lau, D. Betto, K. Borisov, J. M. D. Coey, P. Stamenov, and K. Rode, *Applied Physics Letters* **106**, 122402 (2015), <http://dx.doi.org/10.1063/1.4913687>.
- [21] D. Betto, N. Thiyagarajah, Y.-C. Lau, C. Piamonteze, M.-A. Arrio, P. Stamenov, J. M. D. Coey, and K. Rode, *Phys. Rev. B* **91**, 094410 (2015).
- [22] D. Betto, K. Rode, N. Thiyagarajah, Y.-C. Lau, K. Borisov, G. Atcheson, M. ic, T. Archer, P. Stamenov, and J. M. D. Coey, *AIP Advances* **6**, 055601 (2016), <http://dx.doi.org/10.1063/1.4943756>.
- [23] M. Žic, K. Rode, N. Thiyagarajah, Y.-C. Lau, D. Betto, J. M. D. Coey, S. Sanvito, K. J. O'Shea, C. A. Ferguson, D. A. MacLaren, and T. Archer, *Phys. Rev. B* **93**, 140202 (2016).
- [24] K. Borisov, D. Betto, Y.-C. Lau, C. Fowley, A. Titova, N. Thiyagarajah, G. Atcheson, J. Lindner, A. M. Deac, J. M. D. Coey, P. Stamenov, and K. Rode, *Applied Physics Letters* **108**, 192407 (2016), <http://dx.doi.org/10.1063/1.4948934>.
- [25] R. J. Soulen, J. M. Byers, M. S. Osofsky, B. Nadgorny, T. Ambrose, S. F. Cheng, P. R. Broussard, C. T. Tanaka, J. Nowak, J. S. Moodera, A. Barry, and J. M. D. Coey, *Science* **282**, 85 (1998), <http://science.sciencemag.org/content/282/5386/85.full.pdf>.
- [26] K. Borisov, C.-Z. Chang, J. S. Moodera, and P. Stamenov, *Phys. Rev. B* **94**, 094415 (2016).
- [27] K. Kummer, A. Fondacaro, E. Jimenez, E. Velez-Fort, A. Amorese, M. Aspbury, F. Yakhou-Harris, P. van der Linden, and N. B. Brookes, *Journal of Synchrotron Radiation* **23**, 464 (2016).
- [28] L. Wollmann, S. Chadov, J. Kübler, and C. Felser, *Phys. Rev. B* **92**, 064417 (2015).
- [29] K. Rode, N. Baadji, D. Betto, Y.-C. Lau, H. Kurt, M. Venkatesan, P. Stamenov, S. Sanvito, J. M. D. Coey, E. Fonda, E. Otero, F. Choueikani, P. Ohresser, F. Porcher, and G. André, *Phys. Rev. B* **87**, 184429 (2013).
- [30] S. Paul, S. Ghosh, and B. Sanyal, *Journal of Physics: Condensed Matter* **26**, 196004 (2014).
- [31] J. Jeong, Y. Ferrante, S. V. Faleev, M. G. Samant, C. Felser, and S. S. P. Parkin, *Nat Commun* **7** (2016).
- [32] P. Stamenov, *Journal of Applied Physics* **111** (2012), <http://dx.doi.org/10.1063/1.3679451>.
- [33] F. Wu, E. P. Sajitha, S. Mizukami, D. Watanabe, T. Miyazaki, H. Naganuma, M. Oogane, and Y. Ando, *Applied Physics Letters* **96**, 042505 (2010), <http://dx.doi.org/10.1063/1.3298363>.
- [34] J. W. F. Dorleijn, *Philips Res. Rep.* **31**, (1976).
- [35] N. Nagaosa, J. Sinova, S. Onoda, A. H. MacDonald, and N. P. Ong, *Rev. Mod. Phys.* **82**, 1539 (2010).
- [36] L. Wollmann, S. Chadov, J. Kübler, and C. Felser, *Phys. Rev. B* **90**, 214420 (2014).
- [37] G. J. Strijkers, Y. Ji, F. Y. Yang, C. L. Chien, and J. M. Byers, *Phys. Rev. B* **63**, 104510 (2001).
- [38] I. Galanakis, P. H. Dederichs, and N. Papanikolaou, *Phys. Rev. B* **66**, 134428 (2002).
- [39] I. Galanakis, P. H. Dederichs, and N. Papanikolaou, *Phys. Rev. B* **66**, 174429 (2002).
- [40] R. Nakajima, J. Stöhr, and Y. U. Idzerda, *Phys. Rev. B* **59**, 6421 (1999).
- [41] B. Henke, E. Gullikson, and J. Davis, *Atomic Data and Nuclear Data Tables* **54**, 181 (1993).
- [42] J. Kübler, A. R. William, and C. B. Sommers, *Phys. Rev. B* **28**, 1745 (1983).
- [43] P. Carra, B. T. Thole, M. Altarelli, and X. Wang, *Phys. Rev. Lett.* **70**, 694 (1993).
- [44] T. Koide, H. Miyauchi, J. Okamoto, T. Shidara, A. Fujimori, H. Fukutani, K. Amemiya, H. Takeshita, S. Yuasa, T. Katayama, and Y. Suzuki, *Journal of Electron Spectroscopy and Related Phenomena* **136**, 107 (2004), progress in Core-Level Spectroscopy of Condensed Systems.
- [45] J. Stöhr and H. König, *Phys. Rev. Lett.* **75**, 3748 (1995).
- [46] P. Bruno, in *Magnetismus von Festkörpern und Grenzflächen*, edited by P. Dederichs, P. Grnberg, and Z. W. (Ferienkurse des Forschungszentrums Jilich, 1993) pp. 24.1–24.28.
- [47] P. Bruno, *Phys. Rev. B* **39**, 865 (1989).
- [48] G. van der Laan, *Journal of Physics: Condensed Matter* **10**, 3239 (1998).
- [49] R. K. Wangsness, *Phys. Rev.* **91**, 1085 (1953).